Electronic Supplementary Information for

Low Cell Voltage Electrosynthesis of Hydrogen Peroxide

Junyu Yan, Jing Xia, and Kai Wang*

The State Key Laboratory of Chemical Engineering, Department of Chemical Engineering,
Tsinghua University, Beijing 100084, China

*Corresponding author email: kaiwang@tsinghua.edu.cn
Fax: +86-010-62788568

The supplementary information is as follows:

1. Transmission electron microscopy (TEM) photo of the ORR electrocatalyst

The Ni-O-C catalyst was observed by a TEM and the photo shows Ni worked as 2-5 nm particles on oxidized carbon black.

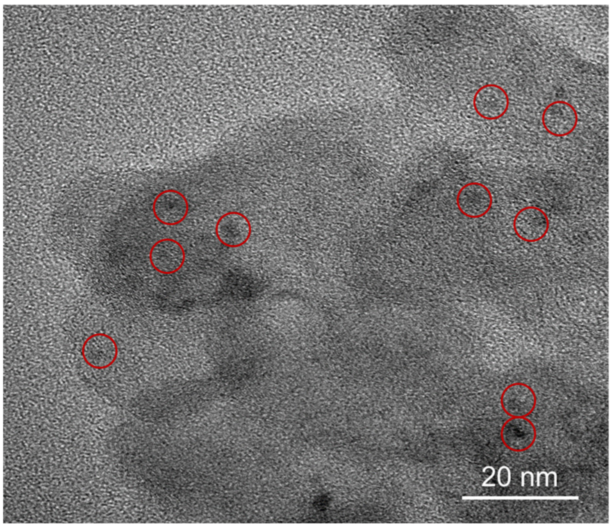

Fig. S1. TEM image of ORR electrocatalyst.

2. Rotating ring-disk electrode test of the electrocatalyst

A typical result of linear sweep voltammetry (LSV) curves is shown in Fig. S2a, where I_{ring} is the ring current and j_{disk} is the disk current density (the disk area is 0.248 cm^2). The selectivity of 2e$^-$ transfer ORR is shown by the Faradaic efficiency (FE) in Fig. S2b, which is calculated by the following equation:

$$\mathrm{FE} = \frac{2I_{\mathrm{ring}}/\mathrm{N}}{I_{\mathrm{ring}}/\mathrm{N} + I_{\mathrm{disk}}} \times 100\% \tag{S1}$$

where N is the collection efficiency, which is equal to 37%; I_{disk} is the disk current.

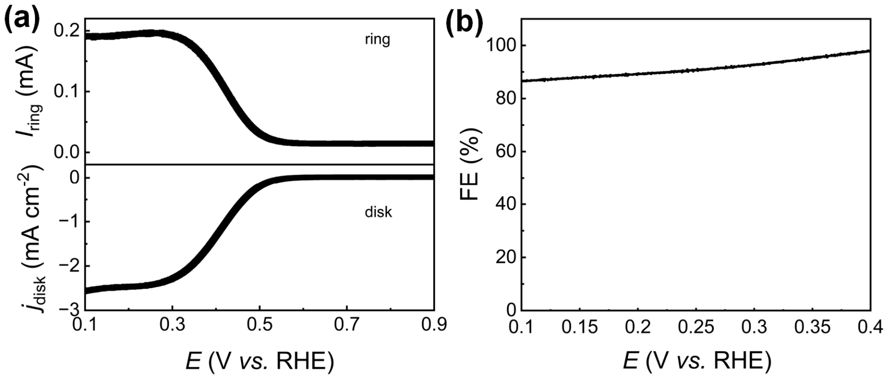

Fig. S2. (a) LSV curves of the Ni-O-C electrocatalyst in 0.05 M Na_2SO_4 aqueous solution at 25°C. The rotation rate is 1600 rpm, and the scan rate is 10 mV s^{-1}. The detected H_2O_2 current on the ring electrode is at a fixed potential of 1.2 V vs. RHE. (b) Faradaic efficiency of 2e$^-$ ORR in 0.05 M Na_2SO_4 electrolyte over the cathodic potential window from 0.1 to 0.4 V vs. RHE.

3. Performance of the Ni-O-C-electrocatalyst under alkaline condition

Typical results of the Ni-O-C-electrocatalyst performance in a KOH condition are shown below.

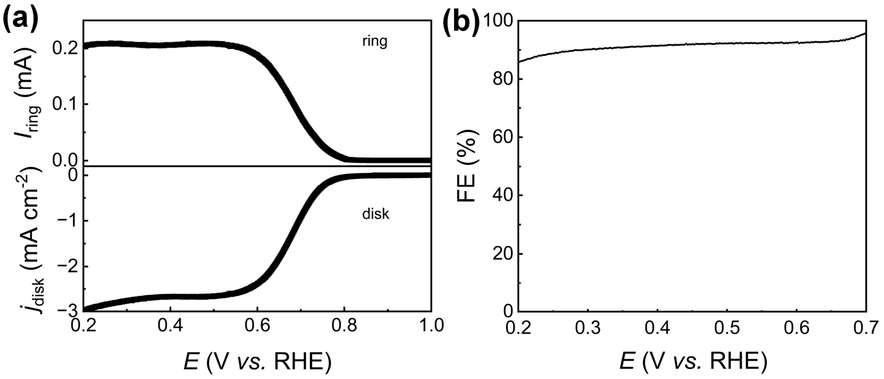

Fig. S3. (a) LSV curves of the Ni-O-C electrocatalyst in 0.1 M KOH aqueous solution at 25°C. The rotation rate is 1600 rpm, and the scan rate is 5 mV s^{-1}. The detected H_2O_2 current on the ring electrode is at a fixed potential of 1.2 V vs. RHE. (b) Faradaic efficiency of 2e$^-$ ORR in 0.1 M KOH electrolyte over the cathodic potential window from 0.2 to 0.7 V vs. RHE.

4. Cathodic morphology

The morphology of cathodic gas diffusion electrode was characterized by a scanning electron microscope (SEM) and an optical camera as shown in Fig. S4. The carbon paper had a porous structure organized by carbon fiber and particles. The electrocatalyst was dripped onto the surface of the carbon particles, which loading amount was 0.2 mg cm^{-2}.

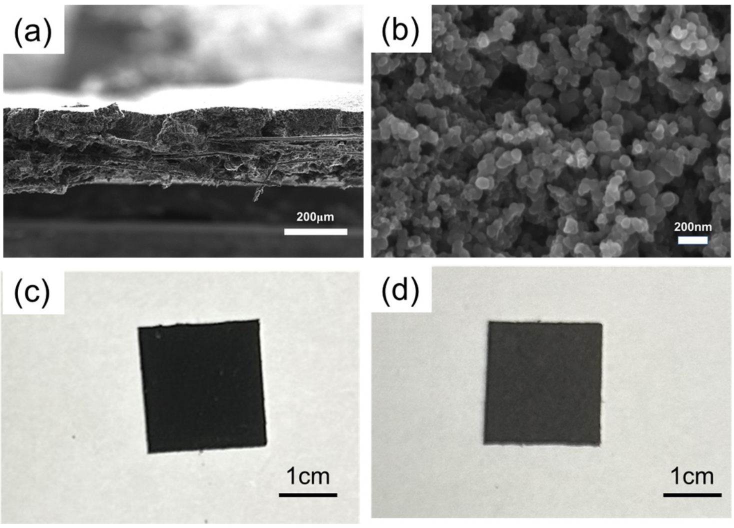

Fig. S4. Pictures of the cathode. (a) SEM image of the carbon paper section. (b) Zoom-in SEM of the cathode surface. (c) Photo of the cathode surface with dripping-loaded electrocatalyst. (d) Photo of the back surface of cathode without electrocatalyst.

5. Anodic morphology

The morphologies of different IrO_2 loaded anodes are shown in Fig. S5. The method to prepare the Ti based electrodes shown in Figs. S5a and S5b was high temperature oxidation sintering of chloroiridium acid. In Fig. S5c, the carbon paper (Sigracet 28 BC) based anode was self-made by dripping IrO_2 particles (Sinero) onto the paper surface.

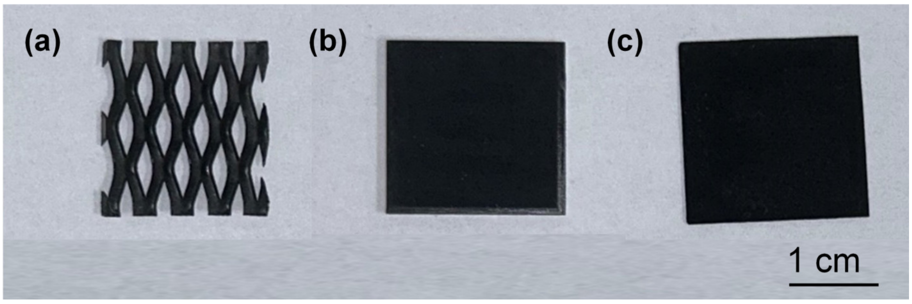

Fig. S5. Photos of (a) IrO_2/Ti mesh, (b) IrO_2/Ti sheet, and (c) IrO_2/carbon paper.

6. Stability test of the ORR catalytic electrode

Continuous experiments were carried out for 2 hours at each current density of 25, 100, 200, 300, and 500 mA cm^{-2}, for totaling 10 hours, as shown in Fig. S6. Under each current condition, the Faradaic efficiency almost remained at 90%.

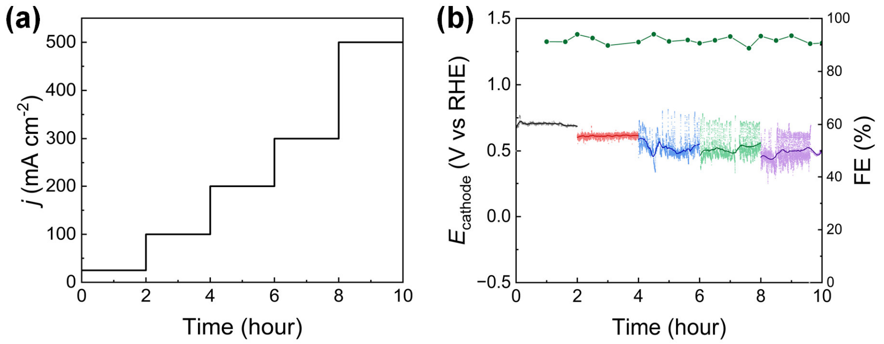

Fig. S6. (a) The curve of applied current-time. (b) The curves of the cathodic potential and Faradaic efficiency. Experiments were conducted at 25°C with O_2 flow rate Q_{O2} = 30 sccm, 0.5 M Na_2SO_4 solution flow rate Q_{Na2SO4} = 1 mL min^{-1} at cathode, and 0.5 M Na_2SO_4 solution flow rate Q_{Na2SO4} = 79 mL min^{-1} at anode. The channel thickness for cathodic solution was 1 mm. Ag/AgCl was used as the reference electrode.

7. Electrochemical impedance spectra (EIS) of the flow cell reactor

In the Nyquist plot, the real part is conventionally denoted as *Z*' (*Z* prime), while the imaginary part is represented by *Z*'' (*Z* double prime). These correspond to the contributions of resistance and capacitance respectively. The intersection of the Nyquist plot with the x-axis reflects the resistance of an electrochemical system. The experiment was conducted by an electrochemical workstation with galvanostatic EIS method. The DC current was 25 mA and the AC current was 0.005 A rms.

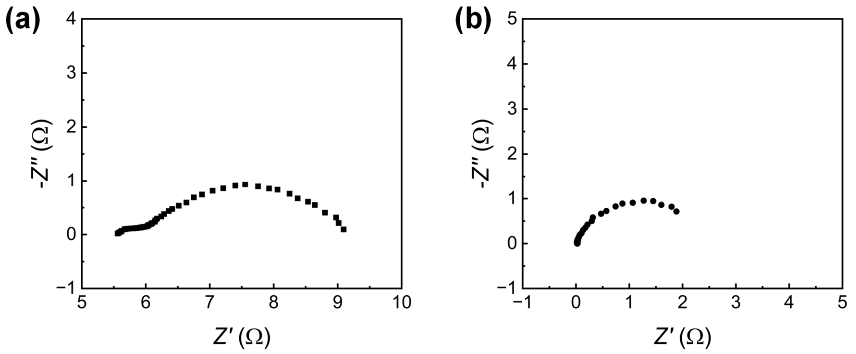

Fig. S7. EIS profiles. (a) Nyquist plot between anode and the reference electrode. (b) Nyquist plot between cathode and the reference electrode.

8. The effect of anodic flow with plate shape anodes

The effect of the anode substrate on the cell voltage and current density is illustrated in Fig. S8. Different substrate materials, as indicated in the figure, influence the expulsion of bubbles from OER, leading to distinct fluctuation behaviors.

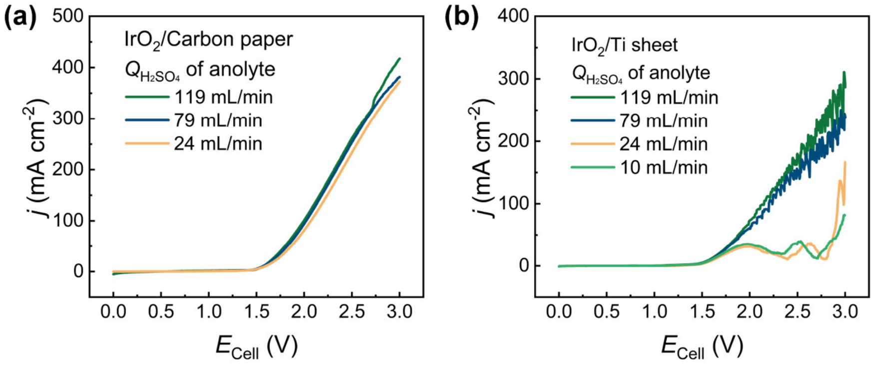

Fig. S8. LSV of the flow cell reactor with different anodic substrate. (a) IrO_2/Carbon paper and (b) IrO_2/Ti sheet. When the anode substrate is titanium sheet, there is a 0.6 mm thick anodic solution channel between the Ti sheet and the membrane. Experiments were conducted at 25°C with Q_{O2} = 30 sccm and Q_{Na2SO4} = 1 mL min^{-1} in cathode. Nafion 117 was used as the membrane.

9. Required oxygen flow rate

Assuming 100% selectivity for the reduction of O_2 to H_2O_2 at 25°C and 1 atm. The relationship of current density and O_2 feeding rate is shown in Fig. S9.

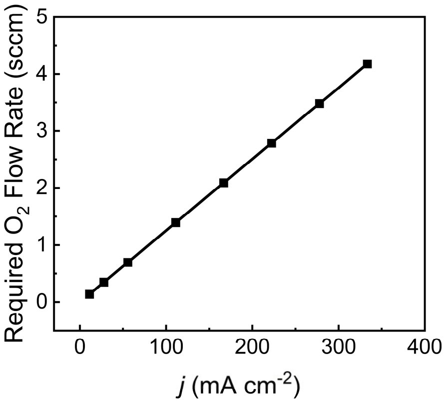

Fig. S9. The required oxygen flow rates at different current densities.

10. Experiment using mixture gas at cathode

When the total flow rate of O_2-N_2 mixture is higher than 20 sccm, the mass transfer of O_2 in the gas diffusion electrode variation is fast enough, and the variation of gas flow rate has little effect on the curves of cell voltage and current density.

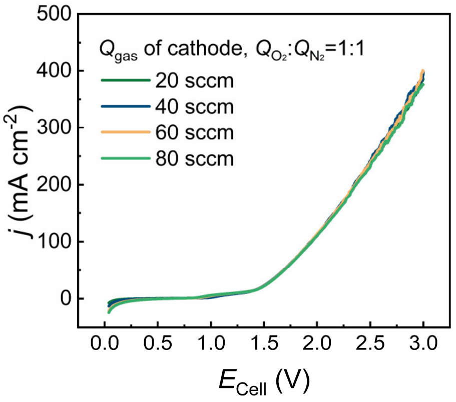

Fig. S10. LSV of the flow cell reactor employing O_2-N_2 mixture. Other experimental conditions are the same with Fig. S6.

11. Activity of OER catalyst in different solutions

The activity of IrO_2/Ti mesh (2 cm × 2 cm) was tested in a 100 mL batch reactor with Ag/AgCl reference electrode and Pt (2 cm × 2 cm) counter electrode. The electrolyte was 0.5 M Na_2SO_4 solution or 0.5 M H_2SO_4 solution. Due to the evolution of O_2, the solution resistance fluctuated. Current interruption iR compensation was therefore employed for real-time compensation of solution resistance. The results showed that the initial potential of ORE was 1.48 V, when we used H_2SO_4 as the electrolyte, but turned to 1.77 V when we used Na_2SO_4 as the electrolyte. (Assuming that the potential at 10 mA is the initial potential)

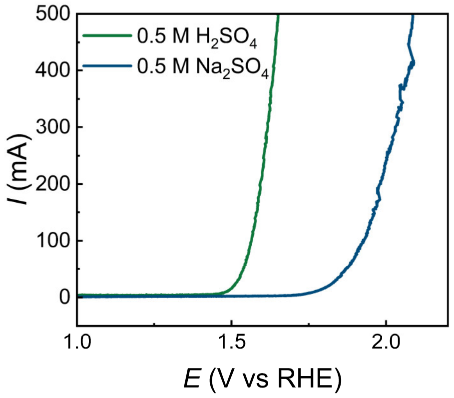

Fig. S11. LSV of the IrO_2/Ti mesh anode in flask reactor. Scan rate was 10 mV s^{-1}

12. Experiment with sticking cathode on membrane

The cathode was directly stuck onto the membrane, and physically compressed in the flow cell. Na_2SO_4 solution and O_2 were mixed through a T-type mixer and entered to the gas channel.

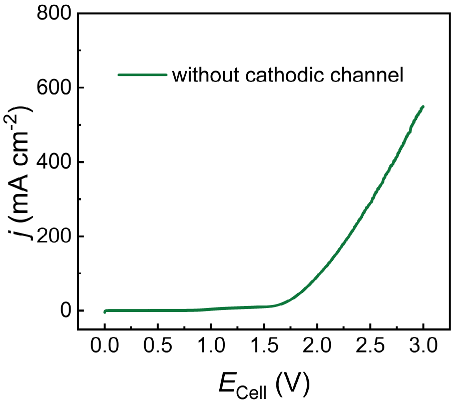

Fig. S12. LSV of the flow cell reactor with cathode stick to the surface of Nafion membrane. Other experimental conditions are the same with Fig. S6. The Faradaic efficiencies were 89.5%, 69.9% and 63.5% at 50, 200, and 400 mA cm^{-2}.

13. Cell voltages and Faradaic efficiencies of the multiple reference electrode experiments

Fig. S13 represents the cell voltages and Faradaic efficiencies in the experiments applying different currents to test the overpotentials of each component. All Faradaic efficiencies are higher than 93% in this test.

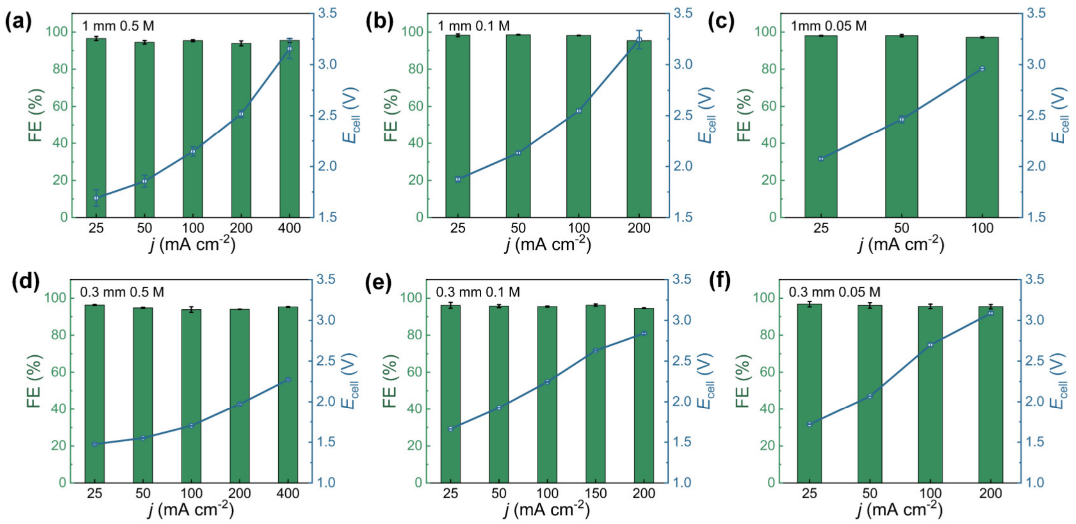

Fig. S13. The cell voltages and Faradaic efficiencies under different thickness of cathodic solution and catholyte concentrations.

14. LSV of the thin cathodic solution channel reactor

The results in Fig. S14 show that the current density was nearly zero when pumping N_2 into the gas channel, but the current density was significant as we pumped O_2 in, which indicated high activity under oxygen reaction conditions.

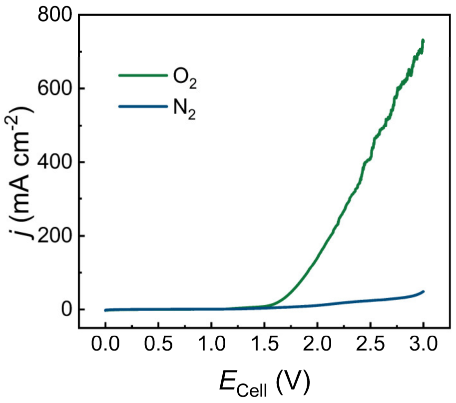

Fig. S14. The LSV of the flow cell reactor with thin cathodic solution channel with different feeding gases.

15. EIS of the improved flow cell reactor

The ESI results in Fig. S15 show that the cell resistance of reactor decreased from the previous 5.6 Ω to 1.6 Ω after optimizing the channel thickness and electrolyte concentration.

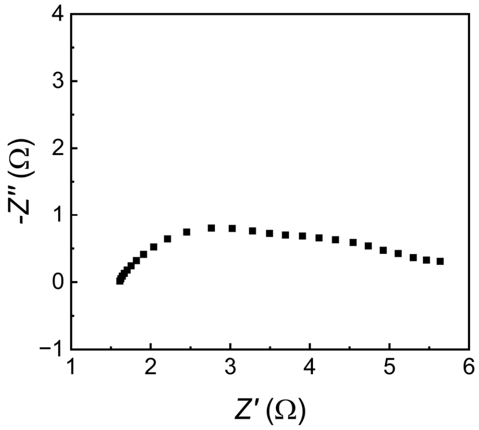

Fig. S15. Nyquist plots of the reactor. Galvanostatic EIS mothod, DC current: 25 mA, AC current: 0.005 A rms. The experiment was conducted at 25°C with cathodic channel thickness=0.3 mm, O_2 flow rate Q_{O2} = 30 sccm, Na_2SO_4 solution flow rate and concentration in cathode Q_{Na2SO4} = 1 mL min^{-1}, C_{Na2SO4} = 0.5 M and H_2SO_4 solution flow rate and concentration in anode Q_{H2SO4} = 2 mL min^{-1} , C_{H2SO4} = 0.5 M. Nafion 117 was used as the membrane.

16. The conversion of MBT-Na

The concentrations of MBT-Na in the reaction solution before and after the oxidation reaction were measured by HPLC, and the conversion of MBT-Na was >99.9%. The small peak at 5.289 min in Fig. 16b should be attributed to the over-oxidized byproduct of MBT. However, this peak is too small to be quantified analyzed.

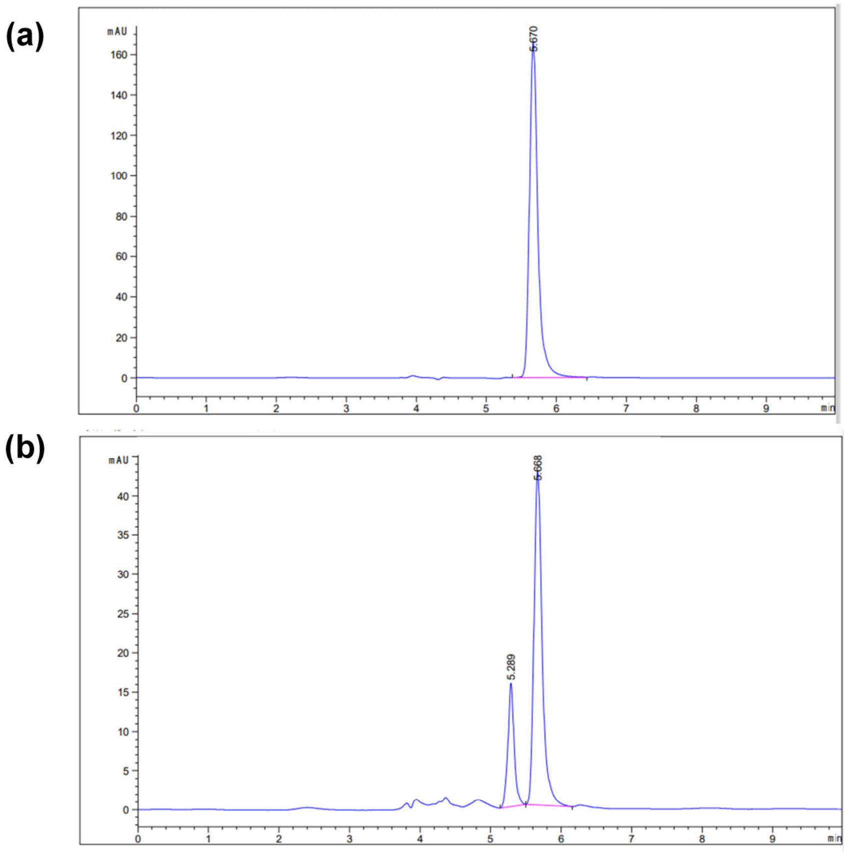

Fig. S16. Concentration analysis of MBT-Na in solutions. (a) The chromatogram of the original MBT-Na solution (0.1 M) after diluting 400 times. (b) The chromatogram of the solution after reaction without any dilution.

17. Summary of cell voltage, current density, and energy consumption in this research and recent literatures

Table S1. Summary of flow cell reactions for the electrosynthesis of H_2O_2.

Electrodes	Catholyte	Current density (mA cm^{-2})	Cell voltage (V)	Faradaic efficiency (%)	H_2O_2 production rate (mmol cm^{-2} h^{-1})	EEC (kWh kg^{-1} H_2O_2)	Ref.
Cathode: Ni-O-C/gas diffusion electrode; anode: IrO_2/Ti, 0.3 mm cathodic solution channel	0.5 M Na_2SO_4	100	1.91	93.9	1.75	3.20	This work
		200	2.12	94.0	3.51	3.56	
		300	2.28	97.1	5.43	3.70	
		400	2.46	95.3	7.11	4.08	
	0.1 M Na_2SO_4	200	2.84	94.6	3.52	4.73	
	0.05 M Na_2SO_4	200	3.09	95.4	3.56	5.11	
Cathode: Co-N-C/gas diffusion electrode; anode: RuO_2/Ti	0.5 M NaCl	50	5.3	95.6	0.89	-	1
Cathode: floating air; anode: mixed metal oxides (MMO)	0.1 M Na_2SO_4	3.8	1.8 (10 cm^2 cathode)	30.2	0.02	8.0	2
		2.02	1.8 (79 cm^2 cathode)	49.2	0.0186	5.4	
		0.85	1.8 (707 cm^2 cathode)	53	0.008	4.9	
Cathode: 4 cm^2 carbon sponge; anode: cylindrical Pt gauze	0.05 M Na_2SO_4	25	4.3V	21	0.1	31.6	3
Cathode: floating air; anode: IrO_2-coated titanium mesh	0.1 M Na_2SO_4	11.11	2.4 V	78	0.15	-	4
Cathode: Co(Pc)-CNT(O); anode: IrO_2/JNT-30A GDL	1 M Na_2SO_4	200	3.1 (IR correction)	90	3.36	-	5
Cathode: 100cm^2 carbon PTFE GDE anode: 100cm^2 DSA	0.05 M Na_2SO_4	50	7.5	73.7	0.688	16.02	6
Cathode: NADE; anode: DSA (IrO_2 coating)	0.05 M Na_2SO_4	20	2.5	86.5	0.29	4.6	7
		60	3.7V	81.8	0.84	6.9	
		120	5.9	71.2	1.44	12.9	
		200	7.97	66.9	2.22	18.9	
Cathode: CoSxPy/MWCNT air diffusion; anode: RuO_2/Ti	0.05 M Na_2SO_4	10	5	60	0.094	17.6	8
		25	9-10	60	0.25	27.9	
		40	13-14	60	0.315	50.8	
Cathode: pitaya peel-derived biochar catalyst; anode: DSA (IrO_2 coating)	0.05 M Na_2SO_4	30	5.5	76.9	0.38	11.33	9
		50	7.6	74.5	0.62	16.15	
		70	9.8	71.3	0.83	21.61	
		100	12.8	65.5	1.09	30.9	

Cathode: oxidized bamboo charcoal; anode: DSA (IrO_2 coating)	0.05 M Na_2SO_4	30	5.6	84.7	0.42	10.4	10
		50	8.4	80.7	0.67	16.5	
		70	10.8	74.8	0.87	22.7	
		100	13.0	70.2	1.17	29.1	
Cathode: CoN_4/VG gas diffusion electrode; anode: DSA	0.1 M $HClO_4$	21	1.8	70	0.304	3.81	11
Cathode: reticulated vitreous carbon cathode; anode: RuO_2/Ti	0.05 M Na_2SO_4 at pH=3	3.5	3.2	30	0.0015	20.4	12
		7	4.5	18	0.0014	61.7	
		10.5	6.0	9	0.0012	153	
Cathode: N doped carbon; anode: IrO_2/Ti	1 M KOH	50	-	-	-	5.0	13
		100	4.3	90	1.68	8.8	
		250	-	-	-	14.16	

Reference

1 Q. Zhao, Y. Wang, W.-H. Lai, F. Xiao, Y. Lyu, C. Liao and M. Shao, *Energy Environ. Sci.*, 2021, **14**, 5444–5456.

2 H. Zhang, Y. Li, G. Li and F. Zhang, *Electrochim. Acta*, 2019, **299**, 273–280.

3 A. Özcan, Y. Şahin, A. Savaş Koparal and M. A. Oturan, *J. Electroanaly. Chem.*, 2008, **616**, 71–78.

4 J. Xu, X. Zheng, Z. Feng, Z. Lu, Z. Zhang, W. Huang, Y. Li, D. Vuckovic, Y. Li, S. Dai, G. Chen, K. Wang, H. Wang, J. K. Chen, W. Mitch and Y. Cui, *Nat. Sustain.*, 2020, **4**, 233–241.

5 B.-H. Lee, H. Shin, A. S. Rasouli, H. Choubisa, P. Ou, R. Dorakhan, I. Grigioni, G. Lee, E. Shirzadi, R. K. Miao, J. Wicks, S. Park, H. S. Lee, J. Zhang, Y. Chen, Z. Chen, D. Sinton, T. Hyeon, Y.-E. Sung and E. H. Sargent, *Nat. Catal.*, 2023, **6**, 234–243.

6 G. R. Agladze, G. S. Tsurtsumia, B.-I. Jung, J.-S. Kim and G. Gorelishvili, *J. Appl. Electrochem.*, 2007, **37**, 375–383.

7 Q. Zhang, M. Zhou, G. Ren, Y. Li, Y. Li and X. Du, *Nat. Commun.*, 2020, **11**, 1731.

8 Z. Ye, D. R. V. Guelfi, G. Álvarez, F. Alcaide, E. Brillas and I. Sirés, *Appl. Catal. B-Environ.*, 2019, **247**, 191–199.

9 S. Wang, H. Liu, D. Ye, Q. Lan, X. Zhu, Y. Yang, R. Chen and Q. Liao, *Sep. Purif. Technol.*, 2022, **289**, 120687.

10 S. Wang, D. Ye, X. Zhu, Y. Yang, J. Chen, Z. Liu, R. Chen and Q. Liao, *Sep. Purif. Technol.*, 2023, **305**, 122397.

11 Z. Lin, Q. Zhang, J. Pan, C. Tsounis, A. A. Esmailpour, S. Xi, H. Y. Yang, Z. Han, J. Yun, R. Amal and X. Lu, *Energy Environ. Sci.*, 2022, **15**, 1172–1182.

12 O. M. Cornejo, I. Sirés and J. L. Nava, *J. Electroanaly. Chem.*, 2020, **873**, 114419.

13 P. Cao, X. Quan, K. Zhao, X. Zhao, S. Chen and H. Yu, *ACS Catal.*, 2021, **11**, 13797–13808.